THE AMERICAN SOCIETY OF MECHANICAL ENGINEERS
345 E. 47th St., New York, N.Y. 10017

96-GT-338

COMPUTATION OF THE UNSTEADY TRANSONIC FLOW IN HARMONICALLY OSCILLATING TURBINE CASCADES TAKING INTO ACCOUNT VISCOUS EFFECTS

B. Grüber and V. Carstens
Institute of Aeroelasticity
DLR
Göttingen, Germany

ABSTRACT

This paper presents the numerical results of a code for computing the unsteady transonic viscous flow in a two-dimensional cascade of harmonically oscillating blades. The flow field is calculated by a Navier-Stokes code, the basic features of which are the use of an upwind flux vector splitting scheme for the convective terms (Advection Upstream Splitting Method), an implicit time integration and the implementation of a mixing length turbulence model.

For the present investigations two experimentally investigated test cases have been selected in which the blades had performed tuned harmonic bending vibrations. The results obtained by the Navier-Stokes code are compared with experimental data, as well as with the results of an Euler method.

The first test case, which is a steam turbine cascade with entirely subsonic flow at nominal operating conditions, is the fourth standard configuration of the "Workshop on Aeroelasticity in Turbomachines". Here the application of an Euler method already leads to acceptable results for unsteady pressure and damping coefficients and hence this cascade is very appropriate for a first validation of any Navier-Stokes code. The second test case is a highly-loaded gas turbine cascade operating in transonic flow at design and off-design conditions. This case is characterized by a normal shock appearing on the rear part of the blades's suction surface, and is very sensitive to small changes in flow conditions. When comparing experimental and Euler results, differences are observed in the steady and unsteady pressure coefficients. The computation of this test case with the Navier-Stokes method improves to some extent the agreement between the experiment and numerical simulation.

INTRODUCTION

For aeroelastic investigations on highly-loaded and oscillating transonic turbomachine blade rows the first essential is the exact knowledge of the unsteady airloads. For this reason much theoretical work has been done in the last decade to develop methods which accurately predict the unsteady pressure, lift and moment coefficients of turbomachinery bladings vibrating in transonic flow.

Until recently, linearized aerodynamic methods have been developed and used as standard tools for routine aeroelastic design studies (Whitehead and Grant, 1980; Verdon and Caspar, 1984; Hall and Crawley, 1989; Kahl and Klose, 1993). Although they meet the requirement of computational efficiency and in many cases produce reasonable results, their range of application is limited to unsteady flows in which strong compressibility and viscosity effects, like large amplitude shock movement and flow separation do not play an essential role.

Further improvement has been gained by the development of nonlinear Euler methods which may be regarded as a first step towards the solution of the Navier-Stokes equations. Fransson (1986) and Gerolymos (1988) were among the first to present a two-dimensional time-marching analysis for solving the non-linearized Euler equations, followed by similar publications of He (1989), Huff (1991), Peitsch et al. (1991) and Carstens (1991). Recently, Gerolymos and Vallet (1994), Peitsch et al. (1994) and Carstens (1994) presented extensions of their methods to three-dimensional flow.

The steadily growing capability of computers to perform arithmetic operations at an increasingly higher speed has stimulated the development of numerical methods for solving the

Presented at the International Gas Turbine and Aeroengine Congress & Exhibition
Birmingham, UK — June 10-13, 1996
This paper has been accepted for publication in the Transactions of the ASME
Discussion of it will be accepted at ASME Headquarters until September 30, 1996

complete set equations for unsteady viscous flow. Since the direct simulation of turbulence lies far beyond the computer capabilities available today, the Reynolds-averaged Navier-Stokes equations are solved together with an appropriate turbulence model. One of the first to provide a code for calculating the unsteady transonic viscous flow in turbomachinery bladings was Rai (1985), who investigated stator-rotor interaction with this method. Further contributions considering the problem of an isolated oscillating blade row have been published by Sidén (1991), Giles and Haimes (1993), He and Denton (1993), Dorney and Verdon (1993) and Abhari and Giles (1995).

The aim of this paper is to provide an insight into the capability of a Navier-Stokes code to predict unsteady aerodynamic coefficients required for flutter investigations. In former calculations of harmonically oscillating suhsonic and transonic turbine cascades with Euler methods it was demonstrated that the measured unsteady pressure and damping coefficients were in some cases well predicted by the computed results, whereas in other cases significant differences were observed (Carstens et. al., 1993). These differences obviously are due to dropping the viscous terms in the governing flow equations, i.e. phenomena such as flow separation and shock-boundary layer interaction cannot be taken into account.

NUMERICAL METHOD

Basic Equations

The strong conservation law form of the unsteady compressible two-dimensional Reynolds-averaged Navier-Stokes equations in transformed coordinates can be written in a non-dimensional form as:

$$\partial_\tau Q + \partial_\xi F + \partial_\eta G = \partial_\xi R + \partial_\eta S \tag{1}$$

with the transformed state vector

$$Q = \frac{1}{J}\begin{bmatrix} \rho \\ \rho u \\ \rho v \\ \rho E \end{bmatrix} , \tag{2}$$

the transformed inviscid fluxes

$$F = \frac{1}{J}\begin{bmatrix} \rho U \\ \rho u U + \xi_x p \\ \rho v U + \xi_y p \\ \rho H U - \xi_t p \end{bmatrix} \quad G = \frac{1}{J}\begin{bmatrix} \rho V \\ \rho u V + \eta_x p \\ \rho v V + \eta_y p \\ \rho H V - \eta_t p \end{bmatrix} , \tag{3}$$

and the transformed viscous fluxes

$$\begin{aligned} R &= \frac{1}{ReJ}\left(\xi_x R_c + \xi_y S_c\right) \\ S &= \frac{1}{ReJ}\left(\eta_x R_c + \eta_y S_c\right) , \end{aligned} \tag{4}$$

where the Cartesian fluxes R_c and S_c are given by

$$R_c = \begin{bmatrix} 0 \\ \tau_{xx} \\ \tau_{xy} \\ u\tau_{xx} + v\tau_{xy} + \\ + \frac{\mu}{Pr(\kappa-1)}\frac{\partial T}{\partial x} \end{bmatrix} ; S_c = \begin{bmatrix} 0 \\ \tau_{xy} \\ \tau_{yy} \\ u\tau_{xy} + v\tau_{yy} + \\ + \frac{\mu}{Pr(\kappa-1)}\frac{\partial T}{\partial y} \end{bmatrix} \tag{5}$$

with

$$\begin{aligned} \tau_{xx} &= \tfrac{\mu}{3}\left\{4\left(\xi_x u_\xi + \eta_x u_\eta\right) - 2\left(\xi_y v_\xi + \eta_y v_\eta\right)\right\} \\ \tau_{xy} &= \mu\left\{\left(\xi_y u_\xi + \eta_y u_\eta\right) - \left(\xi_x v_\xi + \eta_x v_\eta\right)\right\} \\ \tau_{yy} &= \tfrac{\mu}{3}\left\{-2\left(\xi_x u_\xi + \eta_x u_\eta\right) + 4\left(\xi_y v_\xi + \eta_y v_\eta\right)\right\} \\ \tfrac{\partial T}{\partial x} &= \xi_x T_\xi + \eta_x T_\eta \\ \tfrac{\partial T}{\partial y} &= \xi_y T_\xi + \eta_y T_\eta \end{aligned} \tag{6}$$

The density, the Cartesian velocity components, the static pressure and the temperature are denoted by ρ, u, v, p and T, while $\kappa = 1.4$ is the ratio of specific heats and μ, Re, Pr are symbols for the dynamic viscosity, the Reynolds number and the Prandtl number. The Jacobian of the transformation is defined as $J = (\xi_x\eta_y - \xi_y\eta_x)$ and U, V are the contravariant velocity components given as follows:

$$\begin{aligned} U &= \xi_t + \xi_x u + \xi_y v \\ V &= \eta_t + \eta_x u + \eta_y v \end{aligned} \tag{7}$$

Assuming a thermally and caloricly perfect gas, the pressure, p, and the temperature, T, are related to the conservative variables Q by the equations

$$p = (\kappa - 1)\,\rho\,(E - \frac{1}{2}(u^2 + v^2)) \;\; ; \;\; T = \kappa\,\frac{p}{\rho} \tag{8}$$

and the specific total energy, E, and specific total enthalpy, H, are then given hy

$$E = \frac{p}{\rho(\kappa - 1)} + \frac{1}{2}(u^2 + v^2) \quad ; \quad H = E + \frac{p}{\rho} \tag{9}$$

By designating physical quantities with a tilde, the non-dimensional variables of Eq. (1) are obtained by referring all geometrical dimensions to the blade-chord length L, introducing a non-dimensional time by $t = \tilde{t}\tilde{a}_0/L$ and scaling the flow variables $\tilde{\rho}$, $\tilde{u}$, $\tilde{v}$ and $\tilde{E}$ as

$$\rho = \frac{\tilde{\rho}}{\tilde{\rho}_0} \;\; ; \;\; u = \frac{\tilde{u}}{\tilde{a}_0} \;\; ; \;\; v = \frac{\tilde{v}}{\tilde{a}_0} \;\; ; \;\; E = \frac{\tilde{E}}{\tilde{a}_0^2} , \tag{10}$$

where index 0 refers to the stagnation quantities and the speed of sound $\tilde{a}$ is related to the pressure and density by $\tilde{a}^2 = \kappa\tilde{p}/\tilde{\rho}$.

The viscous coefficients are scaled according to

$$\mu = \frac{\tilde{\mu}}{\tilde{\mu}_0} \; ; \; Re = \frac{\tilde{\rho}_0 \, L \, \tilde{a}_0}{\tilde{\mu}_0} \; , \tag{11}$$

where the laminar viscosity μ is calculated by Sutherland's law. For turbulent flows the algebraic turbulence model of Baldwin-Lomax (1978) is used, i.e. μ is replaced by $\mu + \mu_t$ and μ/Pr is replaced by $\mu/Pr + \mu_t/Pr_t$, with $Pr = 0.72$ and $Pr_t = 0.9$.

Flux Vector Splitting of the Inviscid Fluxes

The numerical scheme has been written in a cell-centered finite-volume formulation where the inviscid fluxes are differentiated according to the so-called AUSM-scheme (Advection Upstream Splitting Method) of Liou/Steffen (1993) described below, while the viscous fluxes are computed with central differences. In contrast to the flux vector splitting methods of Steger/Warming (1981) and van Leer (1982), the AUSM scheme is characterized by a separate splitting of the convective and pressure terms of the inviscid fluxes. The numerical flux vector F^*, e.g., is computed at a cell interface $i + \frac{1}{2}$ as

$$F^*_{i+\frac{1}{2}}(Q_L, Q_R) =$$

$$\sqrt{\xi_x^2 + \xi_y^2} \left\{ \frac{1}{2} M_{i+\frac{1}{2}} \left(\begin{bmatrix} \rho a \\ \rho a u \\ \rho a v \\ \rho a H \end{bmatrix}_L + \begin{bmatrix} \rho a \\ \rho a u \\ \rho a v \\ \rho a H \end{bmatrix}_R \right) - \right.$$

$$\left. - \frac{1}{2} |M_{i+\frac{1}{2}}| \left(\begin{bmatrix} \rho a \\ \rho a u \\ \rho a v \\ \rho a H \end{bmatrix}_R - \begin{bmatrix} \rho a \\ \rho a u \\ \rho a v \\ \rho a H \end{bmatrix}_L \right) \right\} +$$

$$+ \begin{bmatrix} 0 \\ \xi_x (p_L^+ + p_R^-) \\ \xi_y (p_L^+ + p_R^-) \\ 0 \end{bmatrix} \; , \tag{12}$$

where L and R designate the left and right value of the state vector with respect to a cell interface. $M_{i+\frac{1}{2}}$, the cell interface Mach number, is obtained by summing up the contributions from the left and right states

$$M_{i+\frac{1}{2}} = M_L^+ + M_R^- \tag{13}$$

with the split Mach numbers M^+ and M^- defined by

$$M^{\pm} = \begin{cases} \pm \frac{1}{4} (M \pm 1)^2 & if \; |M| \leq 1 \\ \frac{1}{2} (M \pm |M|) & otherwise \end{cases} \; , \tag{14}$$

where M from Eq. (14) is the contravariant Mach number $M = U/a$.

The pressure p, is calculated in a similar way as

$$p = p_L^+ + p_R^- \; , \tag{15}$$

where p^+ and p^- are obtained by

$$p^{\pm} = \begin{cases} \frac{1}{4} p (M \pm 1)^2 (2 \mp M) & if \; |M| \leq 1 \\ \frac{1}{2} p (M \pm |M|)/M & otherwise \end{cases} \tag{16}$$

As the dissipative term of the flux balance is given by the second term of Eq. (12), the dissipation vanishes for zero Mach numbers, which leads to accurate results in boundary layers, where the physical viscosity must not be falsified by a too high amount of numerical viscosity.

Time Integration and Spatial Discretization

The method of time integration is the approximately factored implicit algorithm by Beam and Warming (1976). In order to make feasible the application of an approximate factorization scheme, the viscous fluxes are split into two parts :

$$R = R_1 + R_2 \quad , \quad S = S_1 + S_2 \; , \tag{17}$$

with R_1 and S_1 consisting of velocity and temperature derivatives merely in the ξ-direction and R_2 and S_2 containing the corresponding terms in the η-direction. A first-order time accurate algorithm in delta form is then given by

$$\left\{ I + \Delta\tau \left(\delta_\xi \left[\frac{\partial F^*}{\partial Q_{L_\xi}} \Delta Q_{L_\xi} \right] + \delta_\xi \left[\frac{\partial F^*}{\partial Q_{R_\xi}} \Delta Q_{R_\xi} \right] - \right. \right.$$

$$\left. \left. - \delta_\xi \left[\frac{\partial R_1}{\partial Q_{A_\xi}} \Delta Q_{A_\xi} \right] \right) \right\} \cdot$$

$$\cdot \left\{ I + \Delta\tau \left(\delta_\eta \left[\frac{\partial G^*}{\partial Q_{L_\eta}} \Delta Q_{L_\eta} \right] + \delta_\eta \left[\frac{\partial G^*}{\partial Q_{R_\eta}} \Delta Q_{R_\eta} \right] - \right. \right.$$

$$\left. \left. - \delta_\eta \left[\frac{\partial S_2}{\partial Q_{A_\eta}} \Delta Q_{A_\eta} \right] \right) \right\}$$

$$= -\Delta\tau \{ \delta_\xi (F^* - R_1 - R_2 - \Delta R_2) + $$

$$+ \delta_\eta (G^* - S_1 - \Delta S_1 - S_2)) \quad , \tag{18}$$

where F^* and G^* are the inviscid numerical fluxes according to Eq. (12). $\Delta Q = Q^{n+1} - Q^n$ is the difference of the state vector between time steps n+1 and n, while the indices L_ξ, R_ξ, A_ξ L_η, R_η, A_η indicate if Q is updated at the cell interface from left(L), right(R) or averaged(A) state vectors in the ξ- or η-direction. Since the fluxes R_2 and S_1 contain derivatives in η- and ξ-direction respectively, they cannot be included in the

factorization algorithm and thus have to be calculated from the previous time-step:

$$\Delta R_2 = R_2^n - R_2^{n-1} \qquad \Delta S_1 = S_1^n - S_1^{n-1} \tag{19}$$

Since the time integration for the harmonic blade motion has been performed with at least 800 (Euler) or 10000 (Navier-Stokes) time steps per period a first order scheme is sufficient to guarantee time accuracy. It was found that a second order accurate time integration does not change the pressure amplitudes or phases for the selected test cases.

The special method for determining Q_L and Q_R is the MUSCL approach (van Leer, 1979) where the state vector at the cell interface is obtained by upwind extrapolation between neighboring cell-centered values. The spatial discretization scheme used for the present investigations is the fully one-sided first/second-order scheme (here in ξ-direction at cell interface $i+\frac{1}{2}$):

$$\begin{aligned} Q_{L_\epsilon} &= Q_i + \frac{\epsilon}{2}(Q_i - Q_{i-1}) \\ Q_{R_\epsilon} &= Q_{i+1} + \frac{\epsilon}{2}(Q_{i+1} - Q_{i+2}) \end{aligned} \tag{20}$$

which is of first- or second-order accuracy for $\epsilon = 0$ or $\epsilon = 1$, respectively. Finally, the averaged cell interface values Q_A required to update the viscous fluxes are computed as

$$Q_{A_\epsilon} = \frac{1}{2}(Q_i + Q_{i+1}) \tag{21}$$

In order to simplify the solution of Eq. (18), the right hand side of this equation is computed with second order differences ($\epsilon = 1$), whereas the left hand side is computed with first order spatial accuracy ($\epsilon = 0$). This procedure yields a block-tridiagonal structure of the discretized implicit equations. It is easy to show that this manipulation does not alter the overall spatial accuracy of the scheme which is of second order.

Boundary Conditions

On the blade's surface the flow velocity is equal to the blade velocity. This means that

$$\begin{aligned} u &= 0 & v &= 0 & &\text{for steady flow} \\ u &= \tfrac{1}{J}(\eta_t \xi_y - \xi_t \eta_y) & v &= \tfrac{1}{J}(\xi_t \eta_x - \eta_t \xi_x) & &\text{for unsteady flow} \end{aligned} \tag{22}$$

Furthermore, adiabatic walls are assumed, which requires a vanishing temperature gradient, and the pressure gradient at the wall is set to zero

$$\left(\frac{\partial T}{\partial n}\right)_{Wall} = 0 \quad ; \quad \left(\frac{\partial p}{\partial n}\right)_{Wall} = 0 \tag{23}$$

Smooth walls are assumed and consequently, the turbulent viscosity $(\mu_t)_{Wall}$ is set to zero.

The implementation of inlet and outlet boundary conditions is accomplished by the method of Chakravarthy (1982) who proposed a quasi two-dimensional approach. Assuming that the in- and outlet boundaries are ξ=const.-lines, only the wave transport along the characteristics in the $\xi - \tau$-plane is taken into account, whereas the flux in the η-direction is regarded as a source term. A description of the special application of this technique to steady and unsteady turbomachinery flow is given by Carstens (1991).

Assuming that the axial flow component is entirely subsonic at the in- and outlet plane of the cascade, boundary conditions for steady flow are established by replacing incoming waves with fixed flow values, i.e. total pressure, total temperature and flow angle are prescribed at the inlet boundary while static pressure is kept constant at the outlet boundary.

Nonreflecting boundary conditions are used for unsteady flow, i.e. incoming waves (three at the inlet, one at the outlet boundary) have to be suppressed which is accomplished by setting their time derivative to zero.

The application of periodic boundary conditions is self-evident with a line-periodic H-grid (see next section), the type of computational mesh which is used here.

GRID GENERATION FOR MOVING BLADES

The grid generation needed to compute the solution of the Navier-Stokes algorithm in a boundary-fitted coordinate system is obtained by a method presented by Carstens (1988). The procedure used is an elliptic grid generation code based on the solution of Poisson equations, the basic feature of which is the possibility to control the line spacing and intersection angle of the grid lines at the physical boundaries.

The type of grid used for the cascade flow calculation is a line-periodic H-grid, where each grid point on the lower channel boundary has its counterpart on the upper channel boundary in the pitchwise direction. Hence an implicit code is easily introduced on the grid and the periodic boundary conditions can be imposed in an implicit manner.

Due to the strong velocity gradient normal to the wall, a viscous flow computation requires a sufficient density of those grid lines which run parallel to solid boundaries. Additionally, the calculation of the outer eddy viscosity coefficient in the Baldwin-Lomax turbulence model is simplified if the grid lines intersecting the wall are orthogonal to the other family of mesh lines. For this reason, a separate "boundary-layer grid" which matches the elliptic grid at its outer boundary has been generated algebraically (**Fig. 1**).

The grid point displacement must be carefully organized for unsteady flow, i.e. for oscillating blades . As the blades

are in relative motion to each other, the total grid has to be deformed to enable it to conform to the new position of the vibrating blades after each time step. An important feature of any unsteady grid generation is the control of the grid point speed in the interior field. For harmonic motions the time-dependent grid is computed by harmonic interpolation (with respect to time) of a set of steady-state grids with different blade amplitudes. An interactive grid generation procedure is used for non-harmonic blade motions. In this case a new grid is calculated with the original grid generation algorithm after each time step, regarding the old mesh as an initial solution and the new position of the blades as changed boundary conditions. Since in the present method the unsteady cascade flow is computed according to the so-called multi-channel method, the number of blade channels in which the flow has to be calculated depends on the oscillation mode of the cascade. Tuned modes with constant amplitude and constant interblade phase angle result in a pitchwise spatially periodic flow where the spatial periodic length is determined by the interblade phase angle Θ. Consequently, an interblade phase angle of $\Theta = 180°$ requires two blade channels to compute the unsteady flow; four channels are sufficient for $\Theta = \pm 90°$ etc.

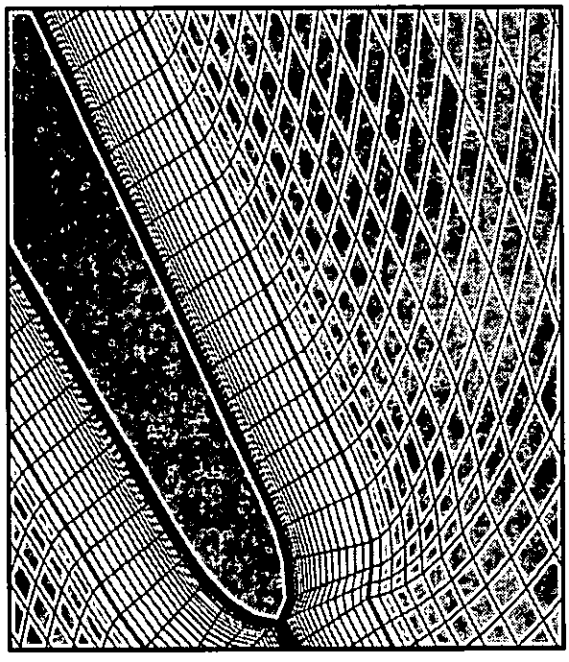

Figure 1: Close up of the grid at the trailing edge

In any other case of vibration mode forcing a non-periodic behavior of flow quantities in the pitchwise direction, the computational domain has to include the complete cascade.

PRESENTATION AND DISCUSSION OF RESULTS

The results for unsteady cascade flow were calculated for two different turbine cascades, namely a steam turbine cascade which has become the Fourth Standard Configuration (STC4) of the "Workshop on Aeroelasticity in Turbomachines" (Bölcs and Fransson, 1986) and a transonic gas turbine cascade known as the TCT3 cascade. Both cascades have been experimentally investigated in the non-rotating annular cascade tunnel of the Swiss Federal Institute of Technology, Lausanne, where the first cascade was run in high subsonic flow at design conditions while the second cascade was investigated in transonic flow at design and off-design conditions.

Unsteady pressure distributions were measured in both cascades for tuned bending modes, i.e., heaving oscillations with the same frequency and amplitude but with a constant controlled interblade phase angle Θ. The reduced frequency ω^* is given by

$$\omega^* = \frac{2\pi f(L/2)}{V_2} \quad , \tag{24}$$

where f, L and V_2 are the vibration frequency, the blade chord length and the cascade outlet velocity, respectively. The interblade phase angle in both cascade configurations is defined as such that it is positive if the phase of the pressure side blade advances to the phase of the regarded blade. The computational mesh for both cascades consisted of a (205x91) grid for Navier-Stokes computations with 27 points in the viscous region and of a coarser (115x27) grid for Euler calculations which have been performed with the AUSM scheme as well as with van Leer flux vector splitting and yield almost identical results. The results presented for inviscid flow are computed with van Leer flux vector splitting. The minimum grid line spacing in the η-direction was chosen as $4 \cdot 10^{-5}$ at the blade's surface which leads to maximum values of 2.0 (STC4) and 1.2 (TCT3) for the non-dimensional wall distance $y^+ = \frac{y}{\mu_w}\sqrt{\rho_w \tau_w}$, where τ_w is the wall shear stress.

Since no information about transition was available from the experimental data, no transition model was incorporated into the code, i.e., the boundary layers along the blade walls were assumed to be fully turbulent. This assumption is supported by several test calculations which were performed a priori with either laminar-turbulent or fully turbulent flow. For the STC4 cascade a change from a laminar-turbulent (prescribed transition at 30 percent of chord length) to a fully turbulent flow does not lead to any differences in the computed pressure distributions. Calculating the design flow through the TCT3 cascade with a laminar-turbulent boundary layer (prescribed transition at 40 percent of chord length) laminar separation is obtained at the leading edge of the blade which indicates that the flow must have been fully turbulent. The off-design flow of this cascade is characterized by a measured separation bubble at the leading edge justifying again the assumption of fully turbulent flow. The geometrical data, the

in- and outlet flow values and the vibration data of both cascades are listed in **Table 1.**

Fourth Standard Configuration

Before comparing the results for unsteady flow, the computed data for steady flow must be validated because they are the starting point for unsteady flow calculations. The steady pressure coefficient is defined here with respect to the inlet flow values

$$c_{p_s} = \frac{p - p_1}{p_{t_1} - p_1} \ , \qquad (25)$$

where p_1 and p_{t_1} denote the measured static and total inlet pressure. **Figure 2** shows the comparison between the experimental and theoretical steady pressure distribution. The agreement is generally good; only small deviations are noticeable at approximately thirty percent of the chord length on the suction side and on the aft portion of the blade's pressure side. It was found that the Navier-Stokes results are sensitive to the grid cell length at the trailing edge of the blade. For this reason the results have been computed with decreasing TECL-values (TECL= Trailing Edge Cell Length), two of which are presented here. The typical overprediction of the acceleration on the front part of the suction side which is confirmed by the computed results of Abhari and Giles (1995), is less pronounced with the smaller cell length of 0.2 percent, a value below which no further changes in the pressure coefficient are observable. A possible explanation for this behavior

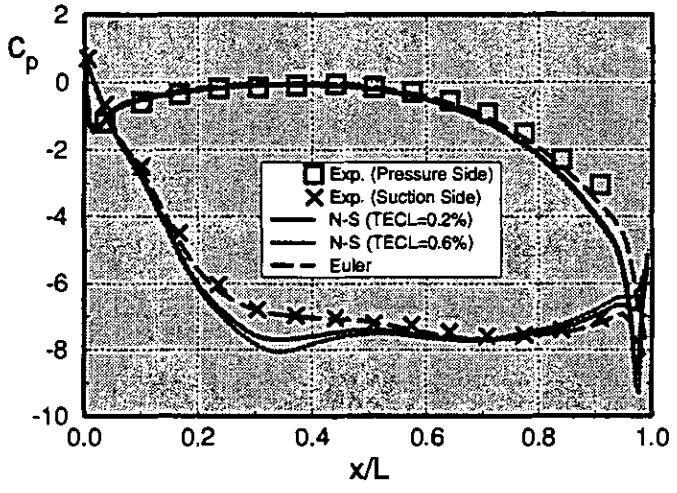

Figure 2: Theoretical and experimental steady pressure distribution, cascade STC4, (TECL=Trailing Edge Cell Length)

is that the coarser grids produce a larger separation region on the pressure side of the trailing edge, which on the other hand, causes a displacement of mass flow to the suction side of the adjacent blade and therefore effect a stronger flow acceleration on tbis part of the blade.

The calculation of the unsteady flow variables for the tuned modes mentioned above has always been performed with the same technique. At rest in steady flow, the blades are started with the prescribed oscillation mode. The calculation is stopped when the peak values of the unsteady lift coefficient for two succesive periods of blade motion do not differ from each other more than 0.1 percent. Since the reduced frequencies for the regarded test cases are low, three or four cycles of blade motion were enough to drive the solution to the desired convergence. By applying a Fourier analysis to

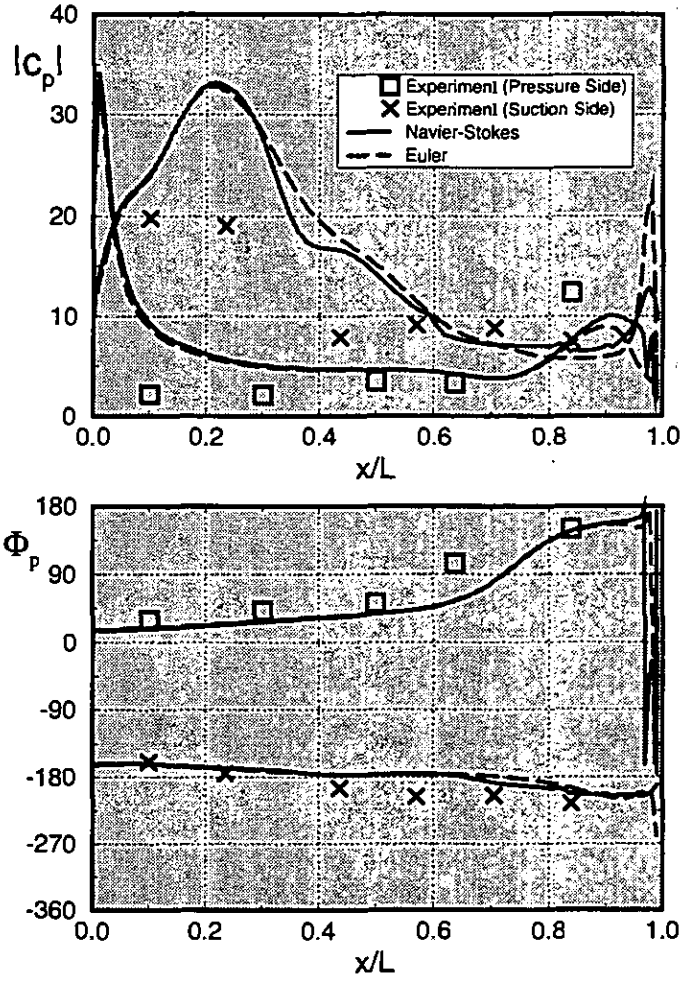

Figure 3: Theoretical and experimental unsteady pressure distribution, cascade STC4, bending motion, $\Theta = 180°$, upper Figure: modulus, lower Figure: phase

the time-dependent values of the last calculated period, the first harmonic of the unsteady pressure and lift coefficients were obtained and compared with the corresponding measured data. Denoting the non-dimensional amplitude of a harmonic bending vibration by y_0/L, the unsteady pressure

coefficient is defined as the complex number

$$c_{p_{ac}} = \frac{\tilde{p}\, e^{i\phi}}{\frac{\rho a}{L}(p_{t_1} - p_1)} \quad , \tag{26}$$

where $\tilde{p}$ and ϕ are the unsteady pressure amplitude and the phase angle with respect to the blade motion.

Figure 3 shows the comparison of the computed with the measured unsteady pressure distributions for the interblade phase angle $\Theta = 180°$. The results of the first harmonics are presented in a module phase diagram. The unsteady pressure data predicted by the Navier-Stokes and Euler code are in reasonable agreement with each other and with the measured ones, except for the peak region of the suction side. Although large discrepancies occur in the front portion of the suction surface, the phase lead or lag of the pressure coefficient with respect to the blade motion is in agreement with the experiment. An important quantity easily obtained by integration of the out-of-phase part of the unsteady pressure coefficient is the aerodynamic damping. In **Fig. 4** this damping coefficient is presented as function of the interblade phase angle. Figure 4 demonstrates the strong influence of Θ on the aerodynamic stability of tuned modes. Vibrations with interblade phase angles in the domain of $+90°$ are clearly damped, whereas significant excitation occurs for Θ-values in the area of $-90°$. The agreement between predicted and measured damping coefficients is good, although the damping at $\Theta = +90°$ is overpredicted.

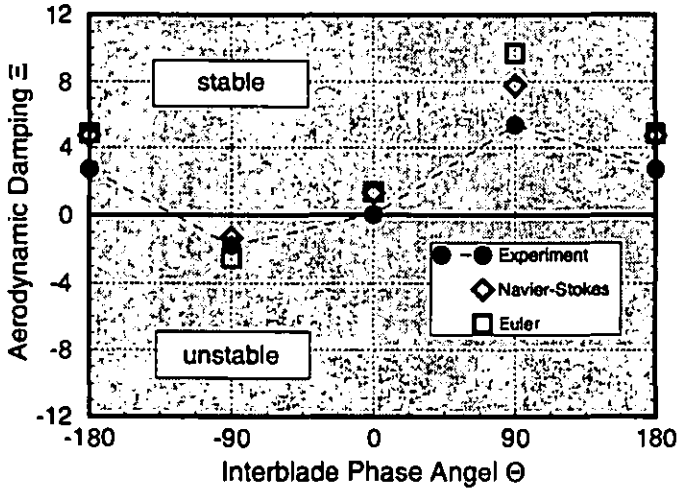

Figure 4: Aerodynamic damping versus interblade phase angel, cascade STC4, bending motion

Transonic Gas Turbine Cascade, Design Flow

This test case is characterized by transonic flow on the suction side of the blade where the supersonic region is terminated by a normal shock at approximately 80 percent of the chord length. The steady pressure distribution is depicted in **Fig. 5**. The pressure coefficient on the pressure side is well predicted by the Navier-Stokes and by the Euler code. As in the previous case, the pressure distribution on the suction side again significantly depends on the fineness of the grid at the trailing edge. Coarser grids effect an upstream movement of the shock due to the displacement of mass flow to the suction side of the blades. Again, for TECL-values below 0.25% no further changes of the flow values are observable.

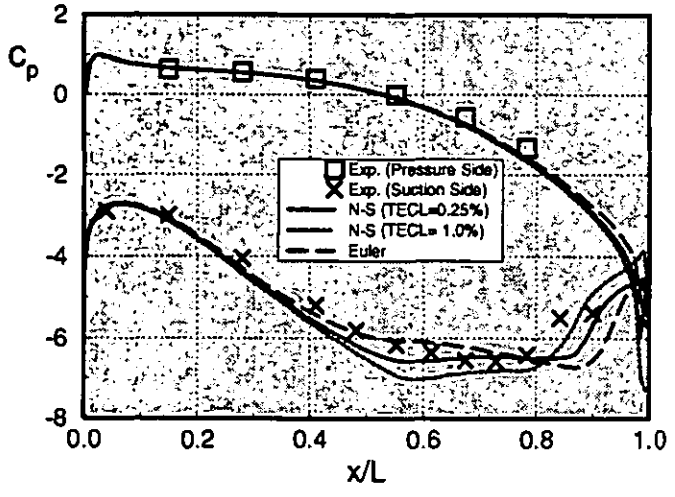

Figure 5: Theoretical and experimental steady pressure distribution, cascade TCT3, design flow, (TECL=Trailing Edge Cell Length)

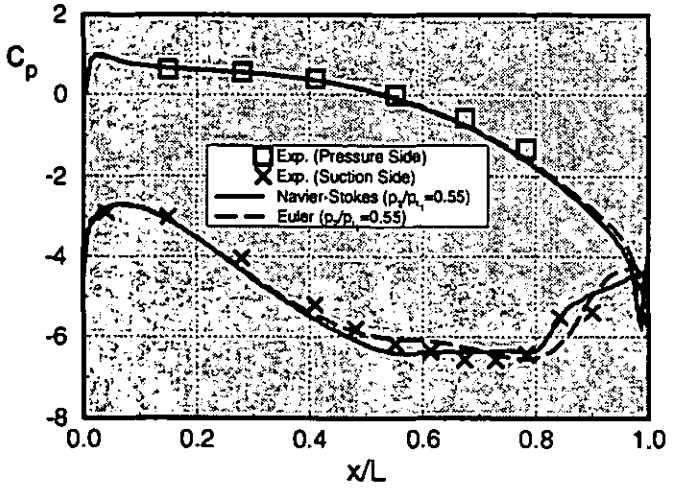

Figure 6: Theoretical and experimental steady pressure distribution, cascade TCT3, design flow, increased exit pressure

In contrast to the Euler results which reproduce the shock position too far behind the measured location, the Navier-Stokes computation predicts a shock position which is mar-

kedly closer to the experimental value. Due to the shock-induced separation bubhle which effects a sudden thickening of the boundary layer, the shock moves upstream since the pressure gradient in front of the shock is fairly small.

In order to investigate the influence of the shock position on the unsteady pressure and lift coefficients, the exit pressure ratio was increased until the predicted shock position was almost identical to the measured one. To achieve this, the exit pressure ratio p_2/p_{t_1} has to be raised from 0.53 to 0.55 (4 percent of its original value). **Figure 6** shows the corresponding steady pressure coefficients of the Navier-Stokes and the Euler calculations. Again, the shock position predicted hy the Euler code is located too far downstream.

In **Fig. 7** the unsteady pressure distributions are plotted for $\Theta = 180°$ and hoth exit pressure values. On the

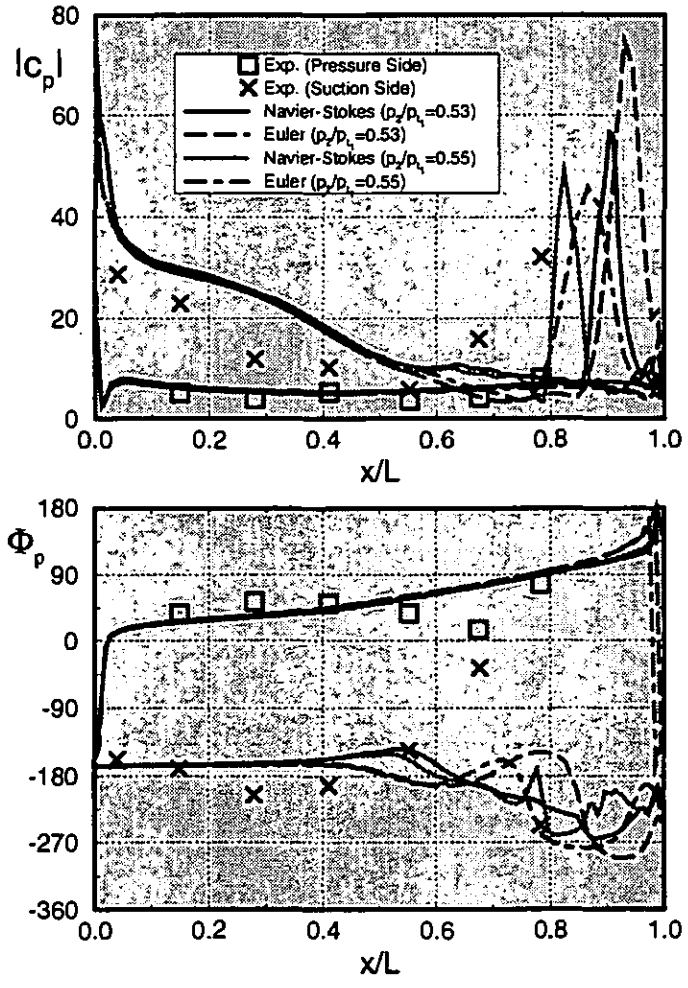

Figure 7: Theoretical and experimental unsteady pressure distribution, cascade TCT3, design flow, bending motion, $\Theta = 180°$, upper Fig.: modulus, lower Fig.: phase

blade's pressure side the Navier-Stokes and Euler results are in good agreement with the experimental data. Furthermore, the unsteady pressure modulus and phase on the suction side are fairly well reproduced in the region in front of the shock, whereas the shock position as well as absolute pressure and phase in the region of the shock are not met satisfactorily hy the theoretical results. When comparing Navier-Stokes and Euler results, the Navier-Stokes code produces the more accurate data with respect to the shock position where the best agreement is obtained with the higher exit pressure ratio p_2/p_{t_1}=0.55.

The aerodynamic damping of the measured and computed results is depicted in **Fig. 8**, where the experimental damping coefficients have been calculated from the measured pressure data. Since the unsteady pressure has been measured with only seven transducers on the suction side (only one transducer in the shock region) and six on the pressure side, the aerodynamic damping can be integrated only with some inaccuracy. The agreement hetween experiment and theory is satisfactory, although the absolute values of damping in the stable and unstable domains are overpredicted by the computed results. A further important result is obtained by comparing the theoretical results obtained for the two different values of p_2/p_{t_1}. Both codes approximately yield the same damping coefficients, the consequence of which is that the shock position in this test case does not essentially influence aerodynamic damping.

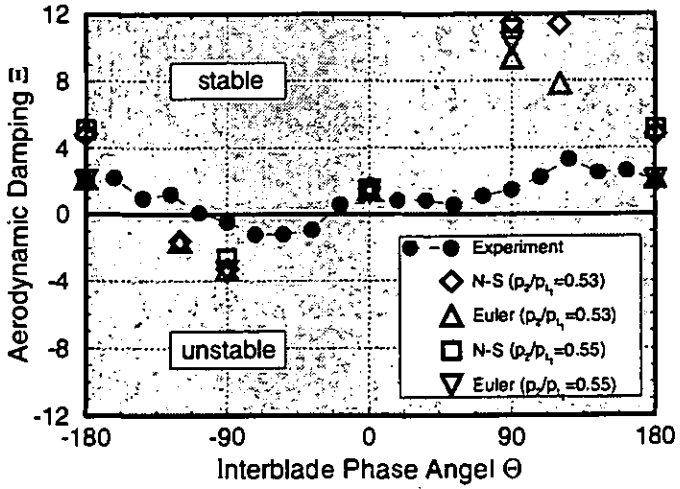

Figure 8: Aerodynamic damping versus interblade phase angel, cascade TCT3, design flow, bending motion

Transonic Gas Turbine Cascade, Off-Design Flow

The experiments for this test case were performed at an off-design inflow angle of $\beta_1 = 33°$, which differs widely from the nominal inlet angle which is given as 15°. From surface paint

flow visualization it can be concluded that a separation bubble exists from the leading edge to approximately 30 percent of the chord length on the suction side. After the separation bubble the flow is accelerated to supersonic values and is recompressed by a normal shock at three quarters of the chord length.

The steady pressure coefficients which are depicted in **Fig. 9** show that the separation bubble is correctly predicted by the Navier-Stokes code, whereas the Euler code, having reached the limit of its performance, produces a large nonphysical suction peak. In comparison to the experiment, both methods predict the shock too far downstream and produce a too high pressure level in front of the shock. Since this pressure level is slightly higher in the Euler results which supports an upstream movement of the shock there exists no observable difference between the Navier-Stokes and Euler data with respect to the shock location. On the pressure side of the blade the computed pressure coefficients are, as in the previous cases, in agreement with the measured data.

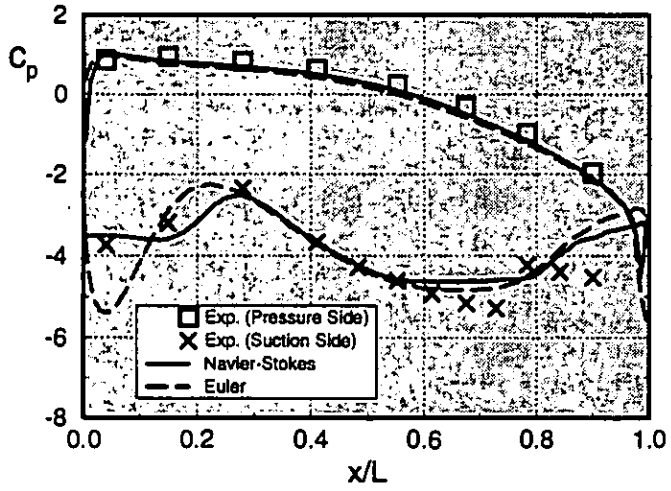

Figure 9: Theoretical and experimental steady pressure distribution, cascade TCT3, off-design flow

Unsteady pressure coefficients for an interblade phase angle of $\Theta = 180°$ are depicted in **Fig. 10**. Here, the modulus, as well as the phase, of the computed unsteady pressure are in good agreement with the experimental values on the pressure side. The same is valid for the region on the suction side ahead of the shock with the exception that the absolute pressure is overpredicted at the position of the separation bubble, whereby the peak value of the Navier-Stokes results is 10 percent of the chord length behind the corresponding peak of the Euler result. At the shock the computed results of absolute pressure are significantly lower than the experimentally determined values, a fact which is explained by the higher calculated steady pressure coefficient in front of the shock.

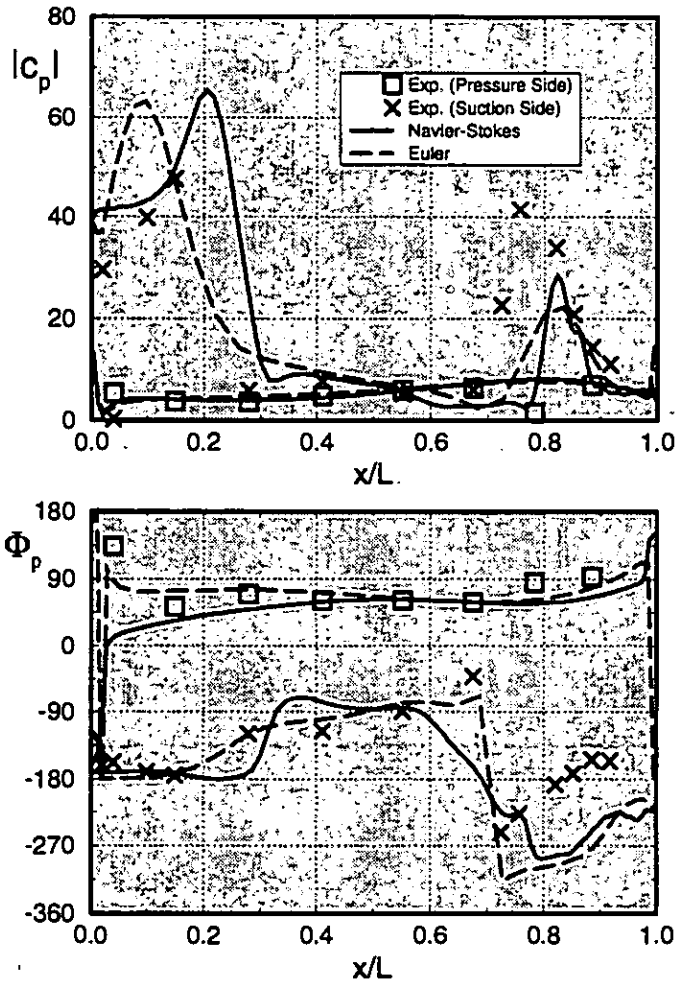

Figure 10: Theoretical and experimental unsteady pressure distribution, cascade TCT3, off-design flow, bending motion, $\Theta = 180°$, upper Figure.: modulus, lower Figure.: phase

Finally, the aerodynamic damping is presented as function of the interblade phase angle Θ in **Fig. 11**. The agreement between theoretical and experimental damping is better than in the case of design flow. Since both codes correctly predict the pressure phase by $\Phi_p \approx 180°$ in the region of the separation bubble, i.e. the unsteady pressure at this position does not contribute to the aerodynamic damping, no larger differences are noticeable when comparing the Navier-Stokes and Euler results. Hence, the separation bubble in this test case does not influence the aerodynamic damping.

CONCLUDING REMARKS

A two-dimensional Navier-Stokes method for computing the unsteady transonic flow through vibrating blade rows has been presented here. The basic features of the existing code are the use of an appropriate upwind discretization of the inviscid fluxes (AUSM scheme), an implicit time integration

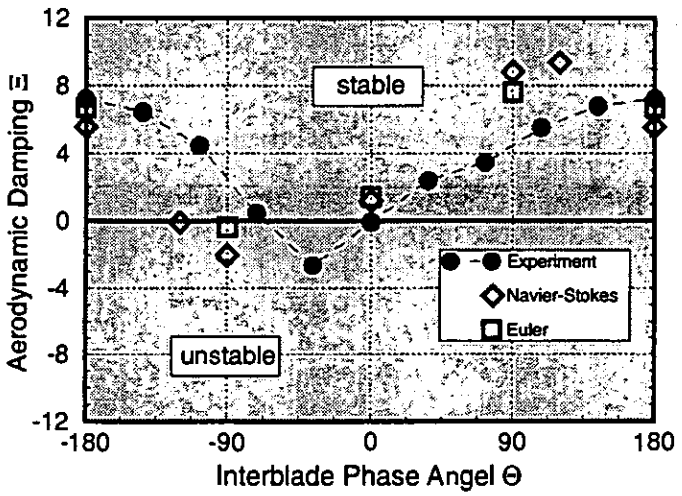

Figure 11: Aerodynamic damping versus interblade phase angel, cascade TCT3, off-design flow, bending motion

of the transformed Navier-Stokes equations which are solved on deforming grids, and of an algebraic turbulence model (Baldwin-Lomax). Steady and unsteady pressure and damping coefficients have been presented for two different turbine cascade configurations which were experimentally investigated for tuned bending modes.

The first configuration which was invesigated, namely the STC4 cascade of the "Workshop on Aeroelasticity in Turbomachines", was merely used for code validation. Comparison between the experimental data of this turbine configuration with the theoretical values clearly shows the capability of the newly developed viscous method to correctly predict unsteady pressure and damping coefficients for non-separated shock-free flow. Additionally, it was shown that the fineness of the grid at the trailing edge considerably influences the steady and unsteady flow on the suction side.

The results of the second test case, the transonic gas turbine cascade TCT3, demonstrate the capability of the new code to simulate flow separation as well as shock boundary layer interaction. This conclusion may be drawn from the Navier-Stokes results for steady flow where the shock position for design flow is predicted markedly closer to the measured location by the viscous method than by the Euler code. Furthermore, the large separation bubble at the leading edge for off-design flow is well reproduced by the Navier-Stokes method. The unsteady pressure and damping coefficients predicted by the new code are in satisfactory agreement with the experimental data for design as well as for off-design flow, but are closer to the Euler results than to the measured data. Finally, it was found that the leading edge flow separation (off-design flow) as well as the shock position have only little influence on the arodynamic damping of the blades.

REFERENCES

Abhari, R. S. ; Giles, M. , 1995, *A Navier-Stokes Analysis of Airfoils in Oscillating Transonic Cascades for the Prediction of Aerodynamic Damping,* ASME Paper, 95-GT-182

Baldwin, B. S. ; Lomax, H. , 1978, *Thin Layer Approximation and Algebraic Model for Separated Turbulent Flows,* AIAA, 78-257

Beam, R.M. ; Warming, R.F. , 1976, *An Implicit Finite-Difference Algorithm for Hyperbolic Systems in Conservation-Law Form,* Journ.Comp.Phys., Vol. 22, pp.87-110

Bölcs, A. ; Fransson, T.H. , 1986, *Aeroelasticity in Turbomachines - Comparison of Theoretical and Experimental Results,* Communications du Lahoratoire de Thermique Appliquée et de Turbomachines, 13, EPFL, Lausanne

Carstens, V. , 1988 *Two Dimensional Elliptic Grid Generation for Airfoils and Cascades,* DLR-FB, 88-52

Carstens, V. , 1991, *Computation of the Unsteady Transonic 2D Cascade Flow by an Euler Algorithm with Interactive Grid Generation,* AGARD CP 507, Transonic Unsteady Aerodynamics and Aeroelasticity, San Diego, USA, October 7-11

Carstens, V. ; Bölcs, A. ; Körbächer, H. , 1993, *Comparison of Experimental and Theoretical Results for Unsteady Transonic Cascade Flow at Design and Off-Design Conditions,* ASME Paper, 93-GT-100

Carstens, V. , 1994, *Computation of Unsteady Transonic 3D-Flow in Oscillating Turbomachinery Bladings by an Euler Algorithm with Deforming Grids,* Proceedings of the 7th International Symposium on Unsteady Arodynamics and Aeroelasticity of Turbomachines, Fukuoka, Japan, September 25-29

Chakravarthy, S.R. , 1982, *Euler Equations - Implicit Schemes and Boundary Conditions,* AIAA Paper 82-0228

Dorney, D.J. ; Verdon, J.M. , 1993, *Numerical Simulation of Unsteady Cascade Flows,* ASME Paper, 93-GT-87

Fransson, T.H. , 1986, *Numerical Investigation of Unsteady Subsonic Compressible Flows Through Vibrating Cascades,* Thesis, Communication du Laboratoire de Thermique Appliquée et de Turbomachines, 12, EPFL, Lausanne

Gerolymos, G.A. , 1988, *Numerical Integration of the Blade-to-Blade Surface Euler Equations in Vibrating Cascades,* AIAA, Vol. 26, pp. 1483-1492

Gerolymos, G.A. ; Vallet, I. , 1994, *Validation of 3D Euler Methods for Vibrating Cascade Aerodynamics,* ASME Paper, 94-GT-294

Giles, M. ; Haimes, R. , 1993, *Validation of a Numerical Method for Unsteady flow Calculations,* Transactions of the ASME, Vol. 115, pp. 110-117

Hall, K.C. ; Crawley, E.F. , 1989, *Calculation of Unsteady Flows in Turbomachinery Using the Linearized Euler Equations,* AIAA, Vol. 27, pp. 777-787

He, L. , 1989, *An Euler Solution for Unsteady Flows Around Oscillating Blades,* ASME Paper 89-GT-279

He, L. ; Denton, J.D. , 1993, *Three Dimensional Time-Marching Inviscid and Viscous Solutions for Unsteady Flows Around Vibrating Blades,* ASME Paper 93-GT-92

Huff, D.L. , 1991, *Unsteady Flow Field Predictions for Oscillating Cascades,* Proceedings of the 6th International Symposium on Unsteady Aerodynamics, Aeroacustics and Aeroelasticity of Turbomachines and Propellers, University of Notre Dame , USA, September 15-19

Kahl, G. ; Klose, A. , 1993, *Computation of the Linearized Transonic Flow in Oscillating Cascades,* ASME Paper 93-GT-269

van Leer, B. , 1979, *Towards the Ultimate Conservative Difference Scheme, V. A Second Order Sequel to Godunov's Method,* Journ.Comp.Phys., Vol.32, pp. 101-136

van Leer, B. , 1982, *Flux Vector Splitting for the Euler Equations,* ICASE Report No. 82-30

Liou, M.S. ; Steffen, C.J.Jr. , 1993, *A New Flux Splitting Scheme,* Journ.Comp.Phys., Vol. 107, pp. 23-39

Peitsch, D. ; Gallus, H.E. ; Kau, H.P. , 1991 *Prediction of Unsteady 2D Flow in Turbomachinery Bladings,* Proceedings of the 6th International Symposium on Unsteady Aerodynamics, Aeroacustics and Aeroelasticity of Turbomachines and Propellers, University of Notre Dame , USA, September 15-19

Peitsch, D. ; Gallus, H.E. ; Weber, S. , 1994, *Computation of Unsteady Transonic 3D-Flow in Turbomachine Bladings,* Proceedings of the 7th International Symposium on Unsteady Arodynamics and Aeroelasticity of Turbomachines, Fukuoka, Japan, September 25-29

Rai, M.M. , 1985 *Navier-Stokes-Simulations of Rotor-Stator Interaction Using Patched and Overlaid Grids,* AIAA Paper 85-1519

Steger, J.L. ; Warming, R.F. , 1981, *Flux Vector Splitting of the Inviscid Gasdynamic Equations with Application to Finite-Difference Methods,* Journ,Comp.Phys., Vol. 40, pp.263-293

Sidén, L.D.G. , 1991, *Numerical Simulation of Unsteady Viscous Compressible Flows Applied to Blade Flutter Analysis,* ASME Paper 91-GT-203

Verdon, J.M. ; Caspar, J.K. , 1984, *A Linear Aerodynamic Analysis For Unsteady Transonic Cascades,* NASA-CR, 3833

Whitehead, D.S. ; Grant, R.J. , 1980, *Force and Moment Coefficients for High-Deflection Cascades,* Proceedings of the 2nd Symposium for Aeroelasticity of Turbomachines, EPFL, Lausanne

	STC4	TCT3 design	TCT3 off-design
chord length L	74 mm	78.5 mm	78.5mm
stagger angle γ	56.6°	41.0°	41.0°
pitch cord ratio τ/L	0.76	0.72	0.72
inflow Mach number M_1	0.28	0.34	0.40
inflow angle β_1	−45°	15°	33°
outflow Mach number M_2	0.90	1.00	0.99
outflow angle β_2	−72°	−58°	−58°
inflow Reynolds number Re_1	$4.2 \cdot 10^5$	$5.7 \cdot 10^5$	$5.7 \cdot 10^5$
bending angle δ (against chord)	60°	90°	90°
vibration amplitude y_0/L	0.0030	0.0050	0.0035
vibration frequency f	150 Hz	210 Hz	212 Hz
reduced frequency ω^*	0.1153	0.1558	0.1545
interblade phase angle Θ	0°, ±90°, 180°	0°, ±18°, ... 180°	0°, ±36°, ... 180°

Table 1: Geometry and operating data of cascades STC4 and TCT3.